ORIGINAL ARTICLE

Multifunctional upconversion–nanoparticles–trismethylpyridylporphyrin–fullerene nanocomposite: a near-infrared light-triggered theranostic platform for imaging-guided photodynamic therapy

Mirong Guan[1], Hao Dong[2], Jiechao Ge[3], Daiqin Chen[1], Lingdong Sun[2], Shumu Li[1], Chunru Wang[1], Chunhua Yan[2], Pengfei Wang[3] and Chunying Shu[1]

Photodynamic therapy (PDT) is an excellent therapeutic modality for various malignant and nonmalignant cancers. This approach utilizes reactive oxygen species generated through the reaction between photosensitizer and oxygen in tissues upon light irradiation to achieve effective treatment. However, limited penetration depth and oxygen-deficient microenvironment hinder the efficiency of PDT. In this work, we design a multifunctional near-infrared (NIR)-triggered theranostic agent based on upconversion–nanoparticles-Polyoxyethylene bis (amine)–trismethylpyridylporphyrin–fullerene nanocomposite (UCNP–PEG–FA/PC$_{70}$) for imaging (fluorescence/upconversion luminescence/magnetic resonance imaging)-guided photodynamic therapy. In this multimodal nanocompsite, UCNPs are employed as light transducers to convert NIR light into ultraviolet–visible light to activate PC$_{70}$ to generate singlet oxygen ($^1O_2$) even under low-oxygen conditions. Meanwhile, the upconversion emission, magnetic resonance imaging and fluorescence signal coming from UCNPs and PC$_{70}$ nanocomposite enable UCNP–PEG–FA/PC$_{70}$ to act as a multimodal imaging diagnostic agent, which facilitates the imaging-guided PDT. Furthermore, folate-mediated active targeting would enhance the accumulation of multifunctional hybrid in tumor. *In vitro* as well as *in vivo* results suggest that this smart nanocomposite is promising as an NIR light-triggered and -targeted theranostic platform for imaging-guided PDT of cancer, which may provide a solution to the bottleneck problems of PDT, namely, limited penetration depth and oxygen-deficient microenvironment.

NPG Asia Materials (2015) **7**, e205; doi:10.1038/am.2015.82; published online 31 July 2015

INTRODUCTION

Theranostic nanoparticles, which combine both therapeutic and diagnostic capabilities in one nanoplatform, have potential to propel the biomedical field toward personalized medicine.[1–3] Specifically, phototriggered theranostics, combining phototherapies (for example, photodynamic,[4,5] photothermal,[6,7] and phototriggered chemo[8,9]/gene therapy[10]) with real-time photodiagnostics (for example, bioluminescence,[11] fluorescence,[12,13] and photoacoustic imaging[14,15]) have been actively pursued due to the advantages of spatiotemporal selectivity, non-ionizing radiation and specificity for disease destruction. Among them, near-infrared (NIR) light-triggered photodynamic theranostics, in which nanoparticles are used as photodynamic therapy (PDT) agents, have recently been receiving much attention due to deep penetration and simultaneous generation of reactive oxygen species (ROS) upon the NIR light irradiation, leading to ablation of

cancer cells as a result. Up to date, several nanocomposites including gold nanocomposites,[16–19] carbon nanostructures,[20,21] W$_{18}$O$_{49}$,[22] WS$_2$,[23] porphyrin-functionalized porous nanoparticles,[24] and upconversion nanoparticles (UCNPs)[25] as NIR light-triggered photodynamic theranostic nanoplatforms have shown efficacy *in vitro* and *in vivo* studies. Wherein, NIR light-triggered photodynamic theranostics based on lanthanide-doped UCNPs has been well investigated for biomedical uses due to their intrinsic anti-Stokes upconversion luminescent properties.[26–28] Compared with traditional optical biomarkers, such as quantum dots and organic dyes, UCNPs exhibit excellent photostability, low background autofluorescence, remarkable penetration depth and high conversion efficiency for NIR photons into visible and ultraviolet (UV) ones, which lead to its unique superiority for bioimaging and bioassay studies.[29,30] In particular, NaGdF$_4$-based UCNPs have been developed as multimodal imaging probes for

upconversion luminescence (UCL) imaging and magnetic resonance imaging (MRI) modality.[31] Such multifunctional nanomaterials offer synergetic advantages of UCL imaging, that is, deep penetration and high sensitivity, along with the anatomic imaging capability of MRI in high spatial resolution.[31] Benefiting from the UV and visible emissions on specific NIR excitation, UCNPs have also been employed as light transducers to activate photosensitizers. UCNP-based PDT nanocomposites are considered promising platforms for cancer therapy due to the non-invasive manner and deep tissue penetration of NIR light, which breaks the dilemma of using UV or visible lights as irradiation source. Since Zhang *et al.*[32] first demonstrated the application of UCNP-based nanocomposite for PDT of bladder cancer cells, recent advances in the integration of UCNPs with PSs such as chlorin e6, Rose Bengal, and IR825 (an NIR-absorbing dye) for their PDT applications *in vitro* and *in vivo* have created many excitements.[33–35] However, the phototoxic effect of $^1O_2$ on PDT is restricted because of a hypoxic condition in tumor tissue.[36] Therefore, it is important to develop NIR light-triggered and -targeted theranostic platform for imaging-guided PDT of cancer under low-oxygen conditions.

Porphyrins as most common used PSs have been approved by Food and Drug Administration for treatment of various non-malignancies and malignancies. They have excellent photophysical properties, such as stronger absorption bands and high singlet oxygen quantum yield because of their large π-conjugated aromatic domains. Strong fluorescence of porphyrin also can be used as imaging probe to monitor the pharmacokinetics.[37] Very recently, trismethylpyridylporphyrin-C$_{70}$ (PC$_{70}$) dyad has been reported to act as a promising photosensitizer for its reasonable water dispersibility, high photostability and favorable biocompatibility.[38] Significantly, the present PC$_{70}$ exhibits extraordinary PDT efficiency *in vitro* even under low-oxygen conditions due to its extremely long lifetime triplet state (211.3 μs).[38] Unfortunately, the UV-to-blue excitation of PC$_{70}$ hinders the enhancement of PDT efficiency *in vivo* due to the limited penetration depth of UV-to-blue irradiation. The introduction of UCNPs may pave the way for the application of PC$_{70}$ as a NIR light-triggered PDT agent *in vivo* since UCNPs can serve as phototransducers by absorbing NIR light to activate PC$_{70}$ to generate $^1O_2$. In addition, the involved UCNPs may reduce the effect by energy transfer from UCNPs to porphyrin,[38] and recover part of the quenched fluorescence of porphyrin.[37]
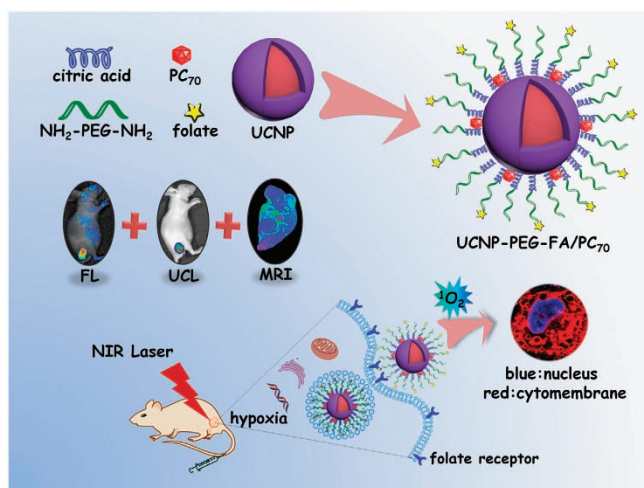

Figure 1 Schematic strategies of trimodal imaging guided UCNP–PEG–FA/PC$_{70}$ (upconversion–nanoparticles–trismethylpyridylporphyrin–fullerene nanocomposite) for photodynamic therapy.

Herein, we design a multifunctional theranostic nanoplatform based on UCNPs/PC$_{70}$ nanocomposite for NIR-triggered fluorescence/UCL/MR trimodal imaging and simultaneous PDT both *in vitro* and *in vivo* (Figure 1). To match the UV-to-blue absorption of PC$_{70}$ for high efficiency of PDT, β-NaGdF$_4$:Yb,Tm@NaGdF$_4$ core/shell nanoparticles were rationally designed. Subsequently, PC$_{70}$ was decorated on the surface of UCNPs through electrostatic interaction. Finally, the UCNPs/PC$_{70}$ nanocomposite was coated with folic acid-modified PEG for active targeting and prolonged circulation time. With such a UCNP–PEG–FA/PC$_{70}$ nanocomposite, trimodal imaging of FL/UCL/MR can be used to guide the PDT treatment of cancer cells efficiently *in vitro* and *in vivo* via the activation of PC$_{70}$ by UV and blue emissions from UCNPs. Besides, folate as a target element can enhance accumulation of nanocomposite in tumor to improve the efficiency of PDT. Most importantly, the synthesized UCNP–PEG–FA/PC$_{70}$ may provide solutions to the bottleneck problems of PDT, namely, limited penetration depth and oxygen-deficient microenvironment.

MATERIALS AND METHODS

Instruments
Samples for transmission electron microscopy (TEM) analysis were prepared by drying a colloidal solution containing nanoparticles on amorphous carbon-coated copper grids. Low-resolution TEM was operated on a JEOL-JEM 2100 transmission electron microscope at 200 kV. High-resolution TEM was carried out on a JEOL-JEM 2100F field emission transmission electron microscope at 200 kV. Powder X-ray diffraction patterns were recorded on a Rigaku D/MAX-2000 diffractometer (Tokyo, Japan) with a slit of 1/2° at a scanning rate of 2° min/min, using Cu Kα radiation ($\lambda = 0.5406$ Å). Upconversion emission spectra were recorded on a Hitachi F-4500 spectrometer, with the Photomultiplier tubes (PMT) voltage of 700 V. The particle size and zeta potential were determined by dynamic light scattering using Malvern Nano-ZS90 apparatus (Malvern Instruments, Worcestershire, UK). Absorbance measurements were carried out using UV2550 spectrophotometer (SHIMADZU, Shimane, Japan). Fluorescence spectra were acquired though Fluorolog spectrophotometer. IR spectra were measured using Thermo instrument (NICOLET In10 MX, Shanghai, China).

Materials
NH$_2$-PEG3000-NH$_2$ and folate were purchased from Innochem (Beijing, China). 1,10-Diamino-4,7-dioxadecane, 1-ethyl-3-(3-dimethylaminopropyl)carbodiimide hydrochloride (EDC) and N-hydroxysuccinimide (NHS) were purchased from Acros (Shanghai, China). The culture medium Dulbecco's modified Eagle's medium (Invitrogen, Shanghai, China) supplemented with 10 % fetal bovine serum (Hyclone Company, South Logan, UT, USA), penicillin (100 μg ml^{-1}) and streptomycin (100 μg ml^{-1}) (Gibco, Grand Island, NY, USA). Dil, MitoRed, Lyso, PI and Hoechst 33258 were purchased from PuJingKangLi (Beijing, China). All other chemicals used were analytical reagents.

Synthesis of β-NaGdF$_4$:Yb,Tm@NaGdF$_4$
The β-NaGdF$_4$:Yb,Tm@NaGdF$_4$ core/shell nanoparticles were synthesized with a modified thermolysis method. Three steps are included as following.

Synthesis of α-NaGdF$_4$:Yb,Tm nanoparticles (α-core). A given amount of Ln(CF$_3$COO)$_3$ (1 mmol), 0.29 mmol Gd(CF$_3$COO)$_3$, 0.70 mmol Yb(CF$_3$COO)$_3$, and 0.01 mmol Tm(CF$_3$COO)$_3$, and CF$_3$COONa (1 mmol) were added to a mixture containing oleic acid (OA), oleylamine (OM), and octadecene (ODE) (40 mmol, molar ratio: 1:1:2) into a three-necked flask (100 ml) at room temperature. The slurry was heated to 110 °C to remove low-boiling water, and oxygen with vigorous stirring under vacuum. Then, the solution was heated to 310 °C at a heating rate of 15 °C min^{-1} and kept for 15 min under N$_2$ atmosphere. After cooling to room temperature, the nanoparticles were collected with centrifugation (7800 r.p.m., 10 min) after precipitation by adding

excess amount of ethanol. The final product was dispersed in 10 ml of cyclohexane.

Synthesis of β-NaGdF$_4$:Yb,Tm nanoparticles (β-core). Five milliliter of as-prepared α-NaGdF$_4$:Yb,Tm nanoparticles were redispersed in a mixture of OA and ODE (40 mmol, molar ratio: 1:1). Then, Ln(CF$_3$COO)$_3$ (0.5 mmol, 0.145 mmol Gd(CF$_3$COO)$_3$, 0.35 mmol Yb(CF$_3$COO)$_3$, and 0.005 mmol Tm (CF$_3$COO)$_3$), and CF$_3$COONa (0.5 mmol) were added. After removing low boiling cyclohexane, water and oxygen with vigorous stirring under vacuum, the mixture was then heated to 325 °C at a heating rate of 15 °C min^{-1} and kept for 60 min under N$_2$ atmosphere. Then, the reaction was cooled to room temperature. Excess amount of ethanol was added to precipitate the nanoparticles, which was collected by further centrifugation (7800 r.p.m., 10 min) and redispersed in 10 ml of cyclohexane.

Synthesis of β-NaGdF$_4$:Yb,Tm@NaGdF$_4$ nanoparticles (β-core@shell). Five milliliter of as-prepared β-NaGdF$_4$:Yb,Tm nanoparticles were redispersed in a mixture of OA and ODE (40 mmol, molar ratio: 1:1). Then, Gd(CF$_3$COO)$_3$ (1 mmol) and CF$_3$COONa (1 mmol) were added. The slurry was heated to 110 °C to remove low boiling cyclohexane, water, and oxygen with vigorous stirring under vacuum. Then, the solution was heated to 320 °C at a heating rate of 15 °C min^{-1} and kept for 40 min under N$_2$ atmosphere. After cooling to room temperature, the nanoparticles were collected with centrifugation (7800 r.p.m., 10 min) after precipitation by adding excess amount of ethanol. The final product was dispersed in 5 ml of cyclohexane.

Preparation of citric acid modified nanoparticles (citric-UCNP)

One milliliter cyclohexane dispersions containing hydrophobic nanoparticles were precipitated with ethanol by centrifugation and redispersed in 5 ml of chloroform. Citric acid (200 mg) was dissolved in 5 ml of deionized water. The pH value of the citric acid solution was tuned ~ 7 by ammonia. Subsequently, the two solutions were mixed under vigorous stirring at room temperature overnight. After that, the chloroform phase was deserted, whereas the water phase was transferred to a centrifuge tube. Citric acid-modified UCNPs were collected after high-speed centrifugation at 18 000 r.p.m. for 15 min and then washed with water for several times. Finally, the products were redispersed in water.

Synthesis of folate-NH-PEG3000-NH$_2$

Folate–NH–PEG3000–NH$_2$ conjugate was synthesized according to the previous method. Briefly, folate was activated with EDC and NHS at a 1:2:2 molar ratio in dimethyl sulfoxide for 2 h. Under nitrogen atmosphere, folate was filtered with a syringe filter (pore size: 0.2 μm). A hetero-bifunctional poly (ethylene glycol) derivate (NH$_2$–PEG3000–NH$_2$ Mw 3000) was added to the above solution at a molar ratio of 15:1 (folate:PEG). After reaction for 4 h under nitrogen atmosphere, the reactants were precipitated with acetone and centrifuged to remove the folate residue. Folate-NH–PEG3000–NH$_2$ conjugation in the supernatant was dialyzed against deionized water.

Synthesis of UCNP-ca/PC$_{70}$ (UCNP/PC$_{70}$)

Citric-UCNP (37.6 mg) was dispersed in water (10 ml). Then 18.8 mg of PC$_{70}$ was added into the above solution and stirred overnight to obtain UCNP/PC$_{70}$.

Synthesis of UCNP–NH–PEG3000–NH–folate/PC$_{70}$ (UCNP–PEG–FA/PC$_{70}$)

Fifteen milligram of EDC and 8.5 mg of NHS were added into the above UCNP/PC$_{70}$ solution and stirred for 2 h. Then, folate–NH–PEG3000–NH$_2$ (500 mg) was added into the above solution, followed by vigorous stirring for 24 h. The nanoparticles were dialyzed by deionized water for 1 week.

Synthesis of PC$_{70}$

In brief, terephthalaldehydic acid methyl ester, pyridine-4-aldehyde and pyrrole were reacted in propionic acid for 1.5 h, and the resultant mixture was separated through a silica gel. Then LiAlH$_4$ was used to reduce the ester group to primary hydroxyl group at room temperature. Subsequently a Swern oxidation reaction was applied to obtain aldehyde group, the final product was purified by silica gel column chromatography. After that, Prato reaction was carried out to obtain crude product which was subjected to silica gel column chromatography. The obtained final product was mixed with methyl tosylate and refluxed in argon atmosphere for 1 h and then passed through an anion-exchange resin repeatedly to yield PC$_{70}$ as a chloride salt.

Loading capacities and release behaviors PC$_{70}$

A gradient concentration (4, 8, 12, 16, 20 and 25%) of PC$_{70}$ in UCNPs solutions was centrifuged at 5000 r.p.m. min^{-1} for 30 min. PC$_{70}$ loading content was calculated according to the following formula: PC$_{70}$ loading content = weight of PC$_{70}$/(weight of PC$_{70}$+weight of UCNPs). The release behavior of PC$_{70}$ from the nanocomposites was evaluated in 10% fetal bovine serum. The resulting solution was filtrated through ultrafiltration (M.W.$_{cut\ off}$ = 10 000) and the filtrate was detected by ultraviolet absorbance spectra.

Detection of singlet oxygen from UCNP–PEG–FA/PC$_{70}$

Water soluble disodium 9,10-anthracendipropionic acid (Na$_2$–ADPA) was used as the ^{1}O$_2$ trapping agent. In the experiments, 100 μl of Na$_2$–ADPA solution (1 mg ml^{-1}) was added into 1.5 ml of UCNP–PEG–FA/PC$_{70}$ solution and then exposed to 980 laser irradiation at a power density of 1 W cm^{-2}. To eliminate the inner-filter effect, the maxima absorption of UCNP–PEG–FA/PC$_{70}$ was adjusted to about 0.2 OD. The absorption of Na$_2$–ADPA from 380 to 420 nm was recorded at different irradiation times.

In vitro PDT

The photo-cytotoxicity of UCNP–PEG–FA/PC$_{70}$ *in vitro* was carried out against luciferase-expression cervical cancer (HeLa-*luc*). Hela-*luc* cells were seeded in a 96-well plate with density of ca. 5×10^4 per well and cultured in 5% CO$_2$ at 37 °C for 24 h. Hela-*luc* cells were then treated with UCNP–PEG–FA/PC$_{70}$ in different concentration gradients for 3 h in the dark, and then irradiated with a 980 nm laser for 10 min (0.8 W cm^{-2}, 1 min break after 1 min irradiation) under air condition and nitrogen condition, respectively. Afterward, the aged medium was replaced with the fresh medium, and cells were cultivated for 24 h in the dark at 37 °C. Cytotoxicity was evaluated by a WST-8 assay with a Cell Counting Kit-8 (CCK-8; DOJINDO, Kumamoto, Japan). A 96-well plate reader (iMarkmicroplate reader, Bio-RAD, Hercules, CA, USA) was used to determine cell viability. Hela-*luc* cells treated only with UCNP–PEG–FA/PC$_{70}$ in the dark for 24 h were used as control. As for other controls, three kinds of cells including Hela-*luc* cells, A549 and HBE cells were treated with either UCNP–PEG/PC$_{70}$ (156 μg ml^{-1}) or PC$_{70}$ (40 μg ml^{-1}, 23.8 μM) and UCNP (80 μg ml^{-1}). Cell viability was then detected. To further confirm the targeting property of UCNP–PEG–FA/PC$_{70}$, folate blocking experiment was done by pre-incubated Hela-*luc*, A549 and HBE cells with folate (40 μg ml^{-1}) for 0.5 h. The cells were further incubated with UCNP–PEG–FA/PC$_{70}$ (200 μg ml^{-1}) for 3 h. Afterward, the cell viability was detected by CCK-8. Corresponding results are expressed as mean ± s.d.

Cell imagings

Hela-*luc* cells were incubated with UCNP–PEG–FA/PC$_{70}$ (200 μg ml^{-1}) at 37 °C, 5% CO$_2$ for 3 h. The aged cell culture was replaced with the fresh Dulbecco's modified Eagle's medium (without phenol red). Subsequently, the cells were illuminated by an external 980 nm (0.8 W cm^{-2}, 1 min break after 1 min irradiation) laser for 10 min. Either Hoechst 33258 (1 mg ml^{-1}, 5 μl, incubated with cells for 20 min), PI (1 mg ml^{-1}, 5 μl, incubated with cells for 15 min), Dil (1 mg ml^{-1}, 5 μl, incubated with cells for 20 min), MitoRed (1 mg ml^{-1}, 5 μl, incubated with cells for 30 min), or Lyso (1 mg ml^{-1}, 5 μl, incubated with cells for 45 min) was then added according to the actual conditions. The cells were washed with icy phosphate-buffered saline buffer for three times before observation. The images were obtained by FV 1000-IX81 confocal laser scanning microscope (Olympus, Miyazaki, Japan). The cells were dyed without laser irradiation as a control.

In vivo PDT

Female Balb/c nude mice (16–20 g) were purchased from Center for Experimental Animals, Institute of Process Engineering, Chinese Academy of Science

(Beijing, China). *In vivo* study conforms to the guidelines of The National Regulation of China for Care and Use of Laboratory Animals. The tumor model was established by subcutaneous injection of Hela/*luc* cells in the right buttock of each mouse. The tumors were allowed to grow for around 5 days to reach the size of ca. 30–60 mm^3.

The tumor-bearing mice were randomized into six groups ($n = 3$, each group). Group 1 was treated by intravenous injection with UCNP–PEG–FA/PC$_{70}$ at a dosage of 200 μl (2 mg ml^{-1}). After 24 h post-injection, the tumor sites were irradiated with 980 nm NIR light for 3 min (0.7 W cm^{-2}, 30 s break after 30 s irradiation). The other three groups were intravenously injected with UCNP–PEG–FA (1.6 mg ml^{-1}, 200 μl), PC$_{70}$ (0.4 mg ml^{-1}, 200 μl), and saline (200 μl), respectively, and followed the same procedure as controls. The fifth and sixth groups were treated with UCNP–PEG–FA/PC$_{70}$ (2 mg ml^{-1}, 200 μl) and saline (200 μl) without laser irradiation as another control. All the groups were treated with only one injection. The body weights and tumor volumes were monitored every 2 days after treatment. The tumor volume was calculated using the following equation: tumor volume (V) = length × width^2/2. Relative tumor volume was calculated as V/V_0 (V_0 was the corresponding tumor volume when the treatment was initiated).

Trimodal FL/UCL/MR imaging *in vivo*

Fluorescence imaging was performed on an *in vivo* imaging system (CRI Maestro 2) with a 600 nm laser as the excited source. The fluorescence images were corrected from 560–800 nm and analyzed with Maestro2 software. The Balb/c nude mice were anesthetized with 1.5% pentobarbital sodium by intraperitoneal injection at dosage of 100 μl. UCNP–PEG–FA/PC$_{70}$ nanoparticles (200 μl, 2 mg ml^{-1}) were injected by intravenous injection, and fluorescence imaging was performed at timed intervals (0, 2, 4, 8, 24 and 72 h).

In vivo UCL imaging experiments were performed with a CALIPER Lumina II *in vivo* imaging system with an adjustable 980 nm laser as the excited source for *in vivo* imaging. Before imaging, the Balb/c nude mice were anesthetized with 1.5% pentobarbital sodium by intraperitoneal injection at dosage of 100 μl. UCNP–PEG–FA/PC$_{70}$ nanocomposites (200 μl, 2 mg ml^{-1}) were injected by intravenous injection, and UCL imaging was performed after 24 h post-injection with exposure time of 0.3 s.

The *in vitro* MR imaging experiments were performed in a 0.5 T MRI magnet (NM120-Analyst, Shanghai Niumag Corporation). UCNP–PEG–FA/PC$_{70}$ nanocomposites were dispersed in water at various Gd concentrations (by ICP measurement). T_1 was acquired using an inversion recovery sequence. Finally, the r_1 value was determined through the curve fitting of $1/T_1$ relaxation time (s^{-1}) versus the Gd concentration (mM).

In vivo MR imaging experiments were performed on a 7 T MRI scanner (Micro MRI, Varian 7T). The tumor-bearing mouse was anesthetized with isoflurane. The mouse was scanned before and after 24 h intravenous injection of UCNP–PEG–FA/PC$_{70}$ nanoparticles (200 μl, 4 mg ml^{-1}).

Histopathological examination

The tissues (heart, liver, spleen, kidneys and lung) were harvested and fixed in a 4% formalin solution. The histopathological tests were performed according to standard laboratory procedures. Tissue samples were numbered and given blind to the pathologist for conventional processing and analysis. Briefly, the tissue samples were embedded in paraffin blocks, sectioned into 5 μm slices, and mounted onto glass slides. The sections were observed after hematoxylin and eosin staining, and photographs were taken using an optical microscope.

RESULTS AND DISCUSSION
Synthesis and characterization of UCNP–PEG–FA/PC$_{70}$

PC$_{70}$ dyad was synthesized according to our previously reported paper.[25] (Supplementary Scheme S1, step 1). To obtain prominent UV–visible emission, NaGdF$_4$:Yb,Tm@NaGdF$_4$ core/shell nanoparticles were prepared as the upconversion energy donor. Moreover, Gd^{3+} ions-based host lattice was employed to support the MRI capability by shortening the relaxtion time of T_1. The synthesis of the core/shell UCNPs was enabled with a modified thermolysis method (Supplementary Scheme S1, step 2).[39,40]

As given in Supplementary Figure S1a, the core and core/shell UCNPs were sphere-like, with high uniformity in size and morphology. After epitaxial growth of the nanoshells (Figure 2a), the mean particle size increased by ~ 20 nm. Furthermore, the high-resolution TEM image of core/cell nanoparticles (Figure 2b) exhibited legible lattice fringes of 0.52 nm, indicating the (10$\bar{1}$0) plane of β-NaGdF$_4$, whereas the successful formation of β-phase UCNPs was also confirmed by the X-ray diffraction patterns (Figure 2d). The upconversion spectra in Supplementary Figure S2 show that the emission intensity of NaGdF$_4$:Yb,Tm@NaGdF$_4$ core/shell UCNPs enhanced 13 times compared with the NaGdF$_4$:Yb,Tm counterpart, indicating the higher upconversion efficiency of the core/shell UCNPs. Afterward, a ligand exchange strategy was employed to transfer the hydrophobic oleate-capped UCNPs to aqueous solutions, where the oleate ligands were replaced by citric acid molecules. As shown in Supplementary Figure S3, no obvious change in size and morphology of the UCNPs occurred after the ligand exchange process. Meanwhile, the emission intensity of Tm^{3+} decreased due to the quenching effect induced by the vibration stretching of hydroxyl groups (Supplementary Figure S4).

Subsequently, water-dispersible and carboxyl-functionalized UCNPs were modified by PC$_{70}$ via electrostatic interactions and then encapsulated by folate-modified polyoxyethylenebis (amine). TEM image shows little change in size of the UCNPs after modification by PEG and PC$_{70}$ (Figure 2c), which may be caused by light atoms with lower contrast compared with that of heavy atoms. Whereas the dynamic light scattering distribution indicates that the hydrated ionic radius is ca. 186 nm, which may ascribe to the free stretching of PEG (Supplementary Figure S5). Further investigation illustrates that the as-prepared UCNP–PEG–FA/PC$_{70}$ nanocomposites are reasonably stable in phosphate-buffered saline, fetal bovine serum and Dulbecco's modified Eagle's medium (Figure 2e), which should mainly attribute to the negative charged property (−15 mV) of UCNP–PEG–FA/PC$_{70}$. The moderate dispersibility facilitates further biomedical applications. The IR spectrum indirectly verifies the formation of amido bond (Supplementary Figure S6). Loading efficiency of PC$_{70}$ was measured as shown in Supplementary Figure S7a, and the result suggested that the loading efficiency is ca. 20%. Release behavior of PC$_{70}$ was also evaluated in 10% fetal bovine serum (Supplementary Figure S7b). PC$_{70}$ could release from the nanocomposite with an amount of ca. 5–7% indicating that the multifunctional composite is reasonably stable under physiological conditions.

Figure 2g reveals that the absorption spectrum of PC$_{70}$ overlaps with the UV emission of UCNPs at 290 nm ($^1I_6$–$^3H_6$), 345 nm ($^1I_6$–$^3F_4$), 361 nm ($^1D_2$–$^3H_6$), and the visible emission at 451 nm ($^1D_2$–$^3F_4$), 475 nm ($^1G_4$–$^3H_6$), indicating that the emissions of UCNPs matched well with the absorption of PC$_{70}$. Hence, PC$_{70}$ can be activated by the energy transfer from UCNPs upon NIR irradiation. To further verify the efficient energy transfer from the UCNPs to PC$_{70}$, the emission spectra of UCNP–PEG–FA nanoparticles incubated with different concentration of PC$_{70}$ were monitored upon 980 nm irradiation. As depicted in Figure 2h, the UV–visible emissions of Tm^{3+} were progressively quenched with elevated addition of PC$_{70}$, whereas the emission of Tm^{3+} at 800 nm ($^3H_4$–$^3H_6$) was almost constant, indicating that the energy transfer indeed occurred between UCNPs and PC$_{70}$ due to the overlap of emission and absorption spectra in UV–visible range. As a result, a slight red-shift of the UV–visible absorption at 428 nm (Figure 2f) and an obvious red-shift of the typical FL spectrum of PC$_{70}$ (Supplementary Figure S8) were observed for UCNP–PEG–FA/PC$_{70}$ due to the interaction between UCNPs and PC$_{70}$. These results indirectly indicate that fluorescence resonance
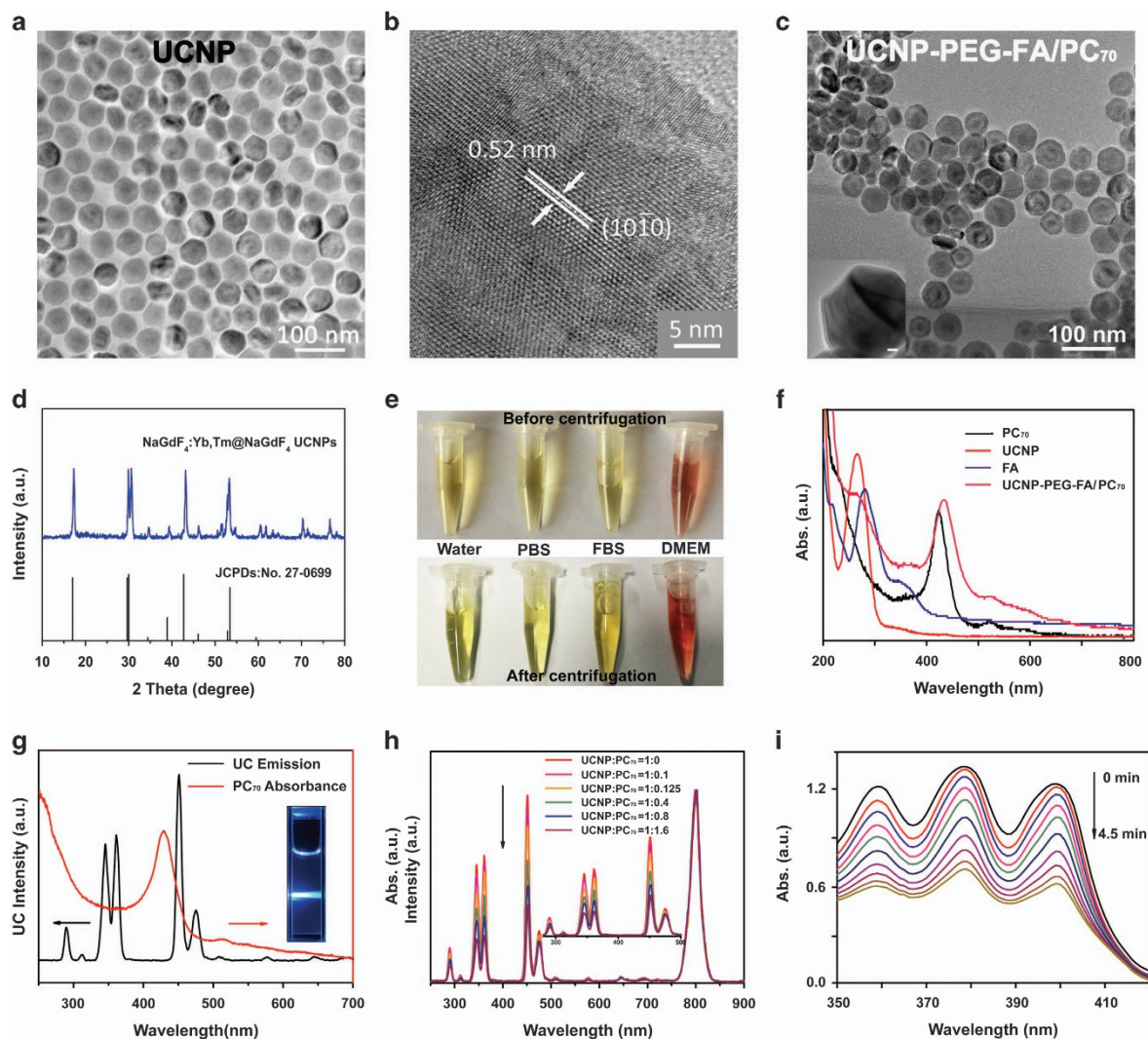
Figure 2 (**a**) Transmission electron microscope (TEM) image of β – NaGdF$_4$:Yb,Tm@NaGdF$_4$ nanoparticles. (**b**) High-resolution TEM image of β – NaGdF$_4$:Yb, Tm@NaGdF$_4$ nanoparticle. (**c**) TEM images of UCNP–PEG–FA/PC$_{70}$ (upconversion–nanoparticles–trismethylpyridylporphyrin–fullerene nanocomposite). Inset is enlarged image and the scale bar is 5 nm. (**d**) X-ray diffraction pattern of as-prepared β-NaGdF$_4$:Yb,Tm@NaGdF$_4$ nanoparticles, consistent with the standard pattern of β-NaGdF$_4$ (JCPDS 06-0342). (**e**) Optical photographs of UCNP–PEG–FA/PC$_{70}$ in water, phosphate-buffered saline, fetal bovine serum and Dulbecco's modified Eagle's medium respectively: before centrifugation (top) and after centrifugation (bottom). (**f**) Absorption spectra of UCNP–PEG–FA/PC$_{70}$, UCNPs, FA and PC$_{70}$. (**g**) Upconversion emission spectrum of UCNPs and absorption spectrum of PC$_{70}$. Inset is the digital luminescence photograph of UCNPs. (**h**) Upconversion emission spectra of UCNP–PEG–FA solutions treated with PC$_{70}$ at different concentrations upon 980 nm irradiation (excitation power was 4 W cm^{-2}). The concentrations of UCNPs in samples are identical. Inset is a local amplification profile of spectra. (**i**) Photodegradation of Na$_2$-ADPA treated with UCNP–PEG–FA/PC$_{70}$ at different time points due to generation of singlet oxygen upon 980 nm irradiation.

energy transfer may exist between UCNPs and PC$_{70}$. Subsequently, the feasibility of UCNP–PEG–FA/PC$_{70}$ for producing $^1O_2$ was investigated by using chemical trapping method (Figure 2i). The result indicates that the photodegradation of Na$_2$–ADPA is time-dependent once treated with UCNP–PEG–FA/PC$_{70}$ and 980 nm irradiation. All of these results indicate that the as-synthesized UCNP–PEG–FA/PC$_{70}$ nanocomposites not only exhibit reasonable stability under physiological conditions but also efficiently produce singlet oxygen upon 980 nm irradiation.

The photodynamic activity *in vitro*
To investigate the NIR light-triggered PDT effect of UCNP–PEG–FA/ PC$_{70}$, the *in vitro* viability assay of Hela-*luc* cells was performed under normal conditions and N$_2$-puring conditions (simulate a low oxygen

condition) as a model. As given in Figure 3a, the cell viabilities decrease gradually with the increase of nanoparticles from 0 to 200 µg ml^{-1} upon 980 nm laser irradiation at a power density of 0.8 W cm^{-2} (480 J cm^{-2}, lower than that of previously reported: 4.5 W cm^{-2}, 10 800 J cm^{-2}),[8] and 90% inhibitory effect on the cell viability was detected at 0.15 mg ml^{-1} of UCNP–PEG–FA/PC$_{70}$. Meanwhile, negligible cytotoxicity against the Hela-*luc* cell was observed in the dark, indicating the favorable biocompatibility of UCNP–PEG–FA/PC$_{70}$ nanocomposites. The same experiments were done under the N$_2$-puring conditions. As shown in Figure 3b, the cell viabilities decrease gradually with the increase of UCNP–PEG–FA/ PC$_{70}$ from 0 to 200 µg ml^{-1} under N$_2$-puring condition, and 50% inhibitory effect on the cell viability was detected at 0.2 mg ml^{-1}. The results indicate that UCNP–PEG–FA/PC$_{70}$ can produce $^1O_2$ under
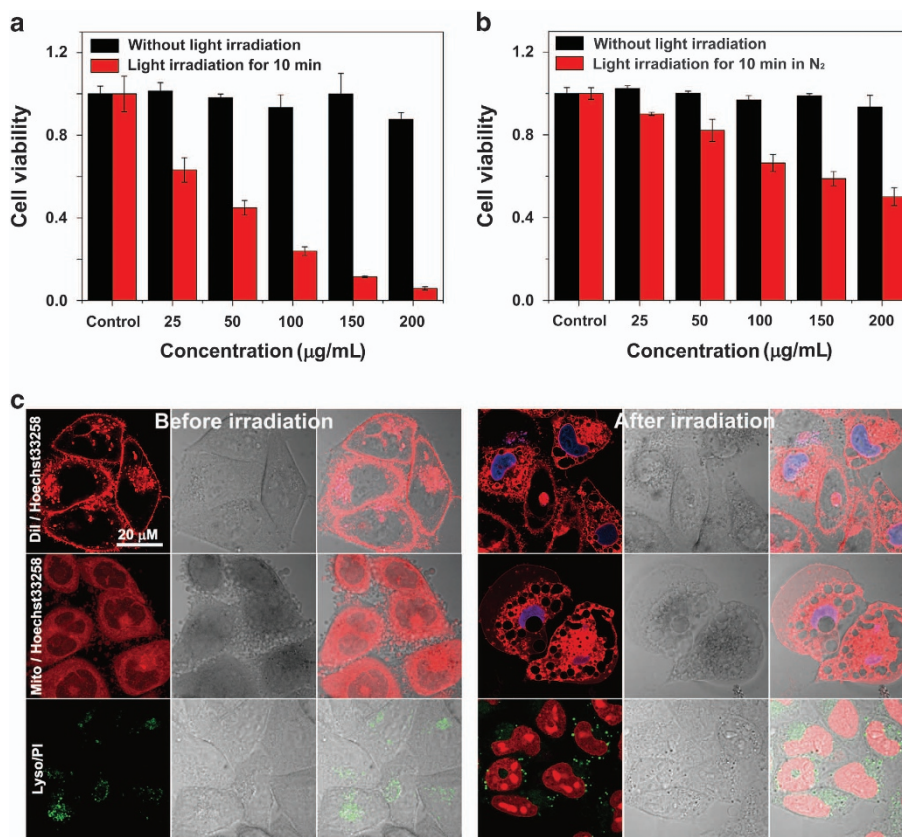
Figure 3 (a) *In vitro* relative viabilities of Hela-*luc* cells incubated with UCNP–PEG–FA/PC$_{70}$ (upconversion–nanoparticles–trismethylpyridylporphyrin–fullerene nanocomposite) at different concentrations, with (red) and without (black) 980 nm NIR light irradiation. (b) Relative viabilities of Hela-*luc* cells under nitrogen-purging conditions incubated with UCNP–PEG–FA/PC$_{70}$ at different concentrations, with (red) and without (black) 980 nm NIR light irradiation. (c) Confocal images before (left) and after (right) NIR light irradiation. First line was stained with DiI and Hoechst 33 258, second line was stained with MitoRed and Hoechst 33 258, third line was stained with PI and Lyso. Each group with three columns represent fluorescence image, optical image and merged image, respectively, from left to right.

low-oxygen conditions, which may be attributable to the formation of (^{3}PC$_{70}$)* with a long triplet lifetime state and thus have enough time to interact with free oxygen.[38]

Several subcellular organelles were stained by related probes and observed under confocal microscope to confirm that the cells were destructed after incubation with UCNP–PEG–FA/PC$_{70}$ and subsequent irradiation with 980-nm NIR light. As shown in Figure 3c, the images in the first row were stained by DiI (cell membrane dye) and Hoechst 33258 (nucleus dye), from which we can see clearly that the cell membrane was bubbling and the nucleus was stained in blue after 980-nm irradiation, indicating that the cell membrane was destroyed and the cells died. The second row was stained by MitoRed tracker (mitochondrial dye) and Hoechst 33258, and the third row was stained by Lyso tracker (lysosome dye) and PI (nucleus dye). The compact mitochondria and lysosomes become incomplete after irradiation, indicating that the subcellular organelles were destroyed by ^{1}O$_2$ generated from UCNP–PEG–FA/PC$_{70}$ after 980 nm irradiation. The lightened subcellular organelles indirectly illustrated that the nanocomposites were internalized into cells and produced intracellular ROS to destroy the subcellular organelles when exposed to NIR light irradiation.

Improved photodynamic activity by conjugation with folate

To reduce the photodynamic damage of synthesized nanoparticles to normal cells and enhance the PDT efficiency toward tumor cells,

folate-modified UCNP–PEG–FA/PC$_{70}$ was designed. As shown in Figure 4a, UCNP–PEG–FA/PC$_{70}$ hybrid exhibits a dramatic decrease in cell viability even at low concentration of 0.2 mg ml^{-1}, whereas UCNPs or PC$_{70}$ alone showed a negligible effect under the same conditions. Moreover, A549 and HBE cells with negative expression of folate receptor were used as controls to evaluate the PDT efficiency. The results indicate that all the above materials including UCNP–PEG–FA/PC$_{70}$ show negligible cytotoxicity toward A549 and HBE cells, suggesting that the superior PDT effect should benefit from the higher binding affinity of the folate-modified nanoprobe to folate receptor overexpressed Hela-*luc* cells.

Competitive inhibition experiment was carried out to further confirm the targeting specificity of UCNP–PEG–FA/PC$_{70}$. UCNP–PEG/PC$_{70}$ (without folate) and UCNP–PEG–FA/PC$_{70}$ blocking with an excess of folate during the incubation were used in PDT treatment as controls. As shown in Figure 4a, UCNP–PEG/PC$_{70}$ exhibited negligible effect on the above three kinds of cells, suggesting that UCNP–PEG/PC$_{70}$ fails to effectively attach to the cell surface at absence of folate. Moreover, the blocking group of UCNP–PEG–FA/PC$_{70}$ reveals that the existence of free folate could inhibit the affinity of UCNP–PEG–FA/PC$_{70}$ to Hela-*luc* cells and therefore effectively preserve the cells from PDT damage (Figure 4b). In addition, confocal imaging experiment was explored to further confirm the above results. Strong red fluorescence could be observed when the Hela-*luc* cells
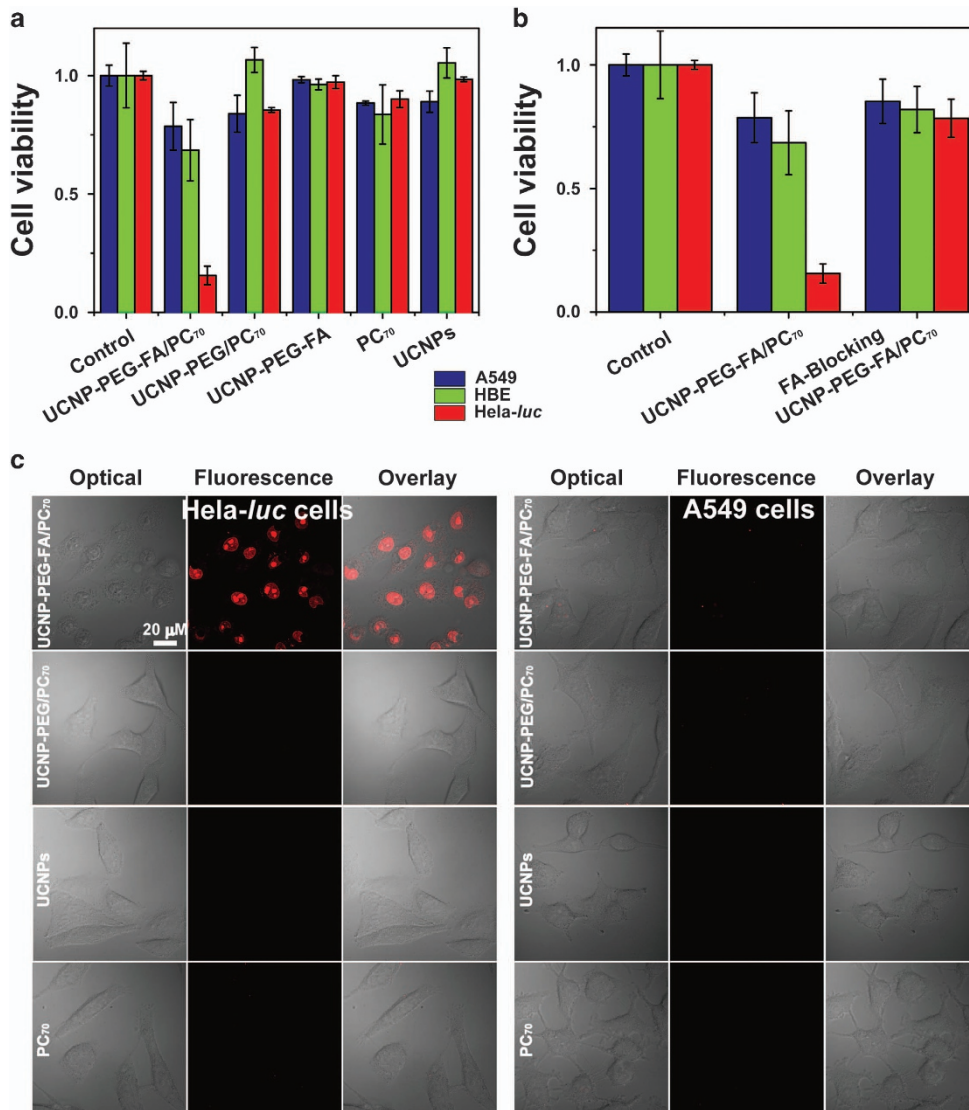
Figure 4 (**a**) The viabilities of three kinds of cells (Hela-*luc*, A549 and HBE cells) incubated with UCNP–PEG–FA/PC$_{70}$ (upconversion-nanoparticles-trismethylpyridylporphyrin-fullerene nanocomposite), UCNP–PEG/PC$_{70}$, UCNP–PEG–FA, PC$_{70}$ and UCNPs respectively. (**b**) The viabilities of three kinds of cells (Hela-*luc*, A549 and HBE cells) incubated with either UCNP–PEG–FA/PC$_{70}$ or the mixture of UCNP–PEG–FA/PC$_{70}$ and an excess of folate. (**c**) Confocal images of PI stained Hela-*luc* cells (left) and A549 cells (right) after photodynamic therapy treatment with UCNP–PEG–FA/PC$_{70}$, UCNP–PEG/PC$_{70}$, UCNP and PC$_{70}$ from top to bottom, respectively.

were treated with UCNP–PEG–FA/PC$_{70}$ and subsequently exposed to 980-nm irradiation and stained by PI. Meanwhile, controls groups (UCNP–PEG–FA/PC$_{70}$-treated A549 cells and UCNP–PEG/PC$_{70}$-, UCNPs- and PC$_{70}$-treated A549 cells, as well as HBE cells and Hela-*luc* cells) exhibited negligible fluorescence under the same conditions (Figure 4c). These results highlight the targeting capability and specificity of UCNP–PEG–FA/PC$_{70}$ nanocomposites toward Hela-*luc* cells via the recognition between folate and folate receptor on the Hela-*luc* cell surface.

Fluorescence/UCL/MR/trimodal imaging

Despite the promising results obtained *in vitro*, one of the most demanding challenges regarding multifunctional platforms still lies in good sensitivity *in vivo* and real-time monitoring for optimized treatment. Herein, the fluorescence intensity *in vivo* was detected to evaluate the real-time biodistribution of UCNP–PEG–FA/PC$_{70}$

nanoparticles. For *in vivo* optical imaging studies, tumor-bearing nude mice were injected with UCNP–PEG–FA/PC$_{70}$ through the tail vein (20 mg kg^{-1}). The resulting fluorescence avoids the autofluorescence from biological tissues and could be used to image the specifics sensitively *in vivo*. From the chronological observation of the images in Figure 5a, we detected the appearance of a rapid tropism associated with the biodistribution of UCNP–PEG–FA/PC$_{70}$ nanoparticles. The fluorescence intensity of UCNP–PEG–FA/PC$_{70}$ in tumor increases to the maximum after 24 h post injection and then decreases with the prolonging time. At the time point of 24 h, the tumor and other organs of the nude mouse injected with UCNP–PEG–FA/PC$_{70}$ were harvested for *ex vivo* imaging to quantify tissue/organ distribution (Figure 5b). The result revealed that distinct fluorescence was presented in tumor site and also in the liver and kidney. By contrast, as given in Supplementary Figure S9, the mouse treated with UCNP–PEG/PC$_{70}$ showed negligible fluorescence after 4 h post-injection. The
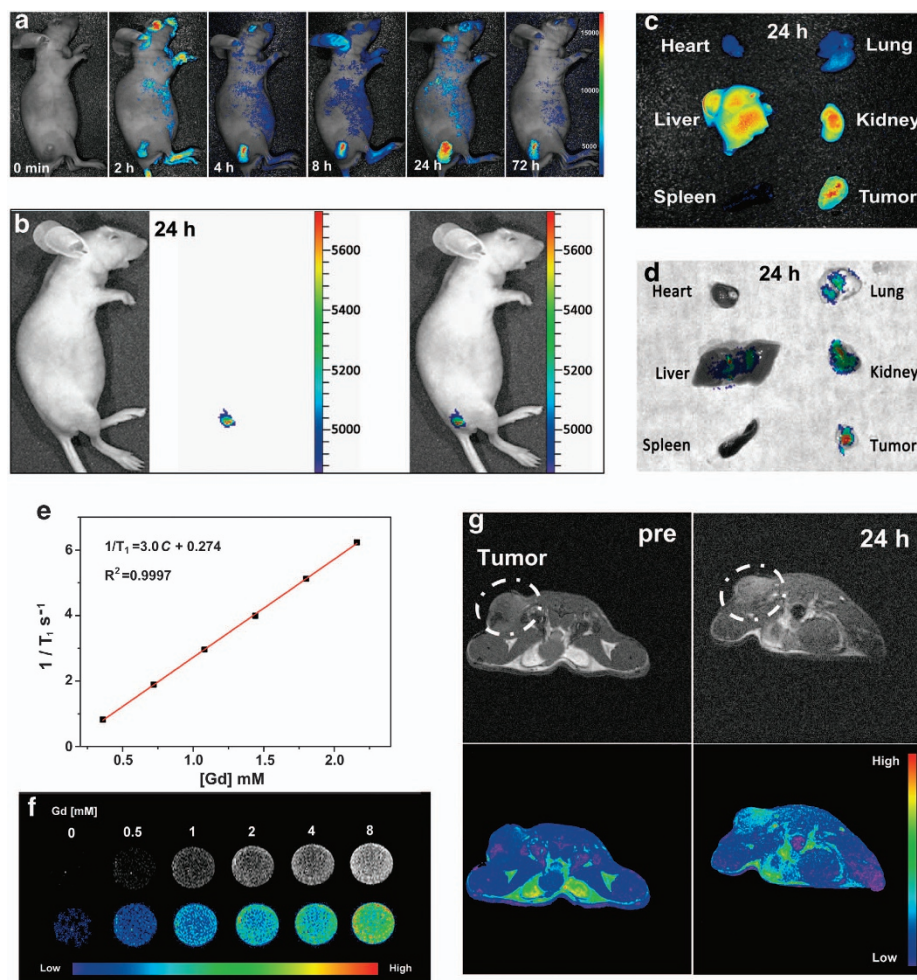
Figure 5 (**a**) *In vivo* fluorescence images of a tumor-bearing mouse at different time points after treatment with UCNP–PEG–FA/PC$_{70}$ (upconversion–nanoparticles–trismethylpyridylporphyrin–fullerene nanocomposite). (**b**) UCL images at the time point of 24 h, and images from left to right represent optical image, UCL image, and merged image. *Ex vivo* images of tumor and other organs after 24 h post-injection: (**c**) fluorescence image and (**d**) UCL image. (**e**) Relaxation rate R_1 versus different molar concentrations of UCNP–PEG–FA/PC$_{70}$ nanoparticles. (**f**) *In vitro* T_1-weighted MR images of UCNP–PEG–FA/PC$_{70}$ at different Gd concentrations. (**g**) *In vivo* T_1-weighted MR image of a tumor-bearing nude mouse: preinjection (left) and after 24-h post injection (right). The color images are treated by pseudo-color.

ex vivo imaging obtained after 24 h post injection (Supplementary Figure S10) indicated the maximal accumulation in the liver and kidney and only a weak fringe of fluorescence located in tumor sites. These results demonstrate that the active targeting of folic and enhanced permeability and retention effect mediated passive targeting play a synergistic role for the accumulation of UCNP–PEG–FA/PC$_{70}$ nanocomposites in tumor. Most interestingly, the real-time fluorescence images not only confirm the feasibility of fluorescence-guided PDT but also contribute to the enhanced efficiency of PDT.

In addition, the emission of UCNPs at 800 nm could be used as the output signal to realize the NIR-to-NIR UCL imaging. The images from left to right in Figure 5c represent the optical image of mouse, UCL image, and their merged images at 24 h post injection, which depict the tumor clearly. The *ex vivo* UCL imaging (Figure 5d) further indicated that UCNP–PEG–FA/PC$_{70}$ mainly accumulated in the liver, spleen and tumor, which were similar to the result from fluorescence image.

To demonstrate the MRI capability of UCNP–PEG–FA/PC$_{70}$, T_1 relaxation time and T_1-weighted MR images at different Gd concentrations were obtained with a 0.5 T MRI scanner. The measured r_1

value was ca. 3.0 mM^{-1} s^{-1} for UCNP–PEG–FA/PC$_{70}$ nanocomposites (Figure 5e), which was comparable to that of clinically used Gd-DTPA (3–4 mM^{-1} s^{-1}) under the same conditions. T_1-weighted MR images (Figure 5f) enhanced with the increase of Gd concentration from 0 to 8 mM. For better visual effect, pseudocolor image was used to enhance the sensitivity. *In vivo* MR imaging was performed for a tumor-bearing mouse with a 7 T MR scanner (Figure 5g). The tumor site was clearly depicted after 24-h post injection, indicating that UCNP–PEG–FA/PC$_{70}$ can be used as a potential T_1 MRI contrast agent. The results from MR image are reasonably consistent with those from fluorescence and UCL images, which also indicate the better tumor targeting performance of UCNP–PEG–FA/PC$_{70}$ as an entity. In a word, the obtained results indicate that UCNP–PEG–FA/PC$_{70}$ could be employed as an efficient and trimodal FL/UCL/MR imaging agent *in vivo* and direct the optimized PDT treatment.

In vivo PDT
The PDT experiments were conducted *in vivo* to evaluate the tumor inhibition efficacy of the UCNP–PEG–FA/PC$_{70}$ with 980 nm NIR light irradiation. The luciferase-expressing cervical cancer cell line Hela-*luc*
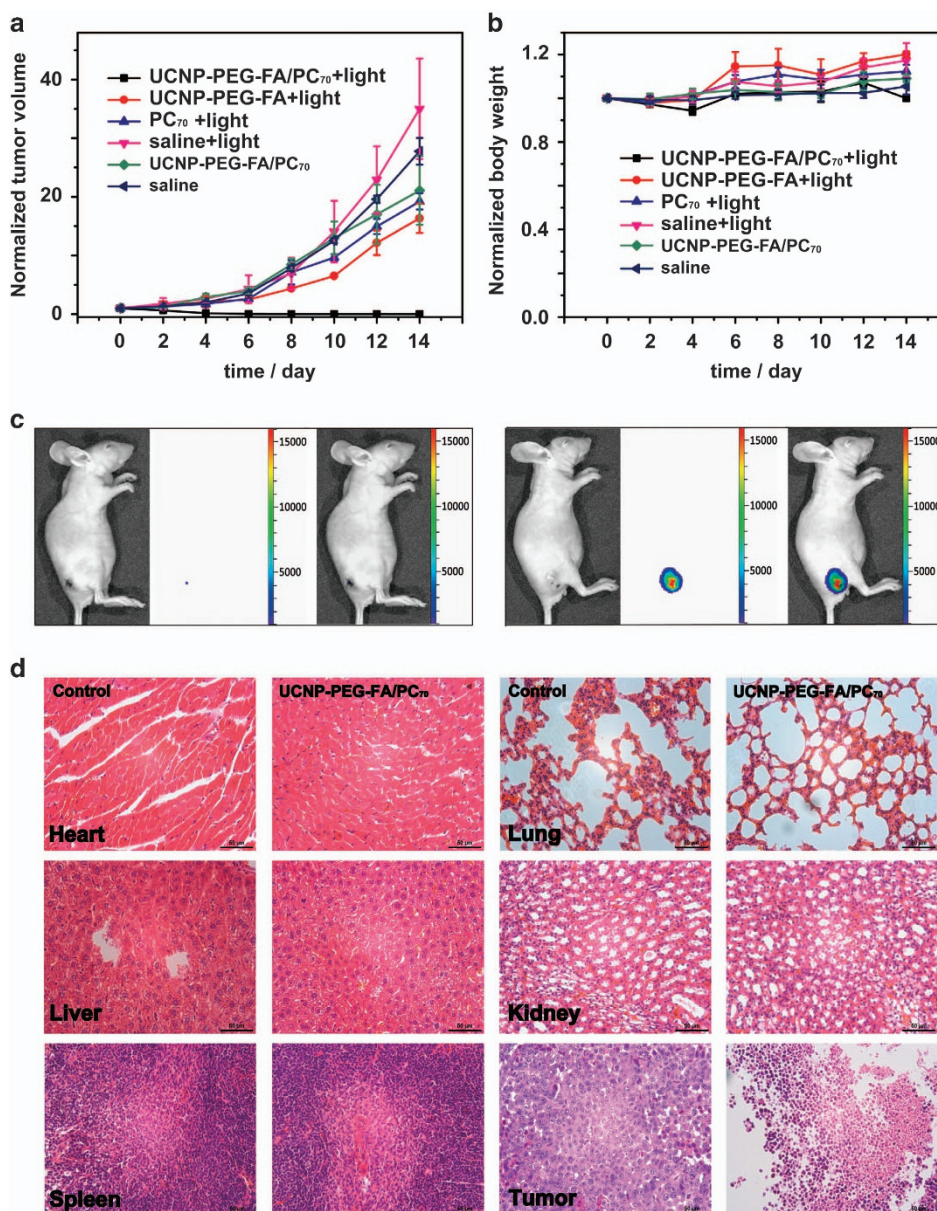
Figure 6 (a) Growth of tumors after treatments. The relative tumor volumes were normalized to their initial sizes. (b) The relative body weights of the nude mice increased continuously after different treatments. Error bars indicate standard deviations; $n=3$. (c) Bioluminescence images of different treatments after 14 days: UCNP–PEG–FA/PC$_{70}$+980 nm NIR light irradiation (left) and saline+980 NIR light irradiation (right). (d) Hematoxylin and eosin stained images of tumors and other organs under different photodynamic therapy treatments.

was selected as the xenograft model, and tumor-bearing nude mice were randomly divided into six groups ($n=3$). The first group was irradiated with 980 nm NIR light (0.7 W cm^{-2}, 126 J cm^{-2}, 30 s break after 30 s irradiation) in the tumor site for 3 min (lower than that of previously reported: 2.5 W cm^{-2}, 30 min, 4500 J cm^{-2})[8] after injection with UCNP–PEG–FA/PC$_{70}$ (2 mg ml^{-1}, 200 μl) for 24 h through caudal vein. In addition, short-interval irradiation method was developed to avoid over-heating by the NIR light. The next three groups were injected with UCNP–PEG–FA, PC$_{70}$, and saline, respectively, and then irradiated under the same conditions as controls. Another two groups injected with either UCNP–PEG–FA/PC$_{70}$ or saline separately without irradiation were used as controls. Figure 6a demonstrates that the group treated with UCNP–PEG–FA/PC$_{70}$+ 980 nm NIR light irradiation exhibited optimal tumor growth

inhibition efficacy. By contrast, the tumors of control groups grew continuously under the same conditions. Meanwhile, the digital photographs of representative mice with neoplasm (Supplementary Figure S11) before and after irradiation for 6 days showed that the tumor sizes of mice treated with UCNP–PEG–FA/PC$_{70}$+980 nm NIR light irradiation were much smaller than those of control groups, as confirmed by the representative bioluminescence images of mice (Supplementary Figure S12) given at the 14th day (Figure 6c). Bioluminescence from the UCNP–PEG–FA/PC$_{70}$+980 nm NIR light irradiation-treated group nearly disappeared compared with saline-treated mice, suggesting that the tumor of treated group was effectively destroyed. Hematoxylin and eosin staining images of main organs and tumor are presented in Figure 6d. The clear separation of the nuclear and cytoplasm confirmed that the tumor cells were destroyed after

treated with UCNP–PEG–FA/PC$_{70}$+980 nm NIR light irradiation. By contrast, tumor from the mouse treated with saline exhibited cramped construction of nuclear and cytoplasm. Importantly, there were no obvious lesions were found in other organs, indicating that UCNP–PEG–FA/PC$_{70}$ has no significant toxicity to organisms. In addition, body weight, as an important parameter to evaluate the systemic toxicity of nanomaterials, did not show abnormal change for all groups (Figure 6b), indicating that UCNP–PEG–FA/PC$_{70}$ nanocomposite does not have obvious adverse side effects.

CONCLUSION

In summary, we have successfully prepared UCNP–PEG–FA/PC$_{70}$ nanocomposite as an NIR light-triggered and targeted theranostic platform for trimodal imaging-guided PDT *in vitro* as well as *in vivo*. The developed UCNP–PEG–FA/PC$_{70}$ nanocomposites have the following advantages: (1) Upon NIR irradiation, UCNPs could convert NIR light into UV-to-visible light to effectively activate PC$_{70}$ to produce $^1O_2$ for killing tumor under low oxygen conditions; (2) Three kinds of imaging methods (FL/UCL/MR) were integrated into one system to provide the complementary information for accurate diagnosis and guide treatment of tumor; (3) Folate-mediated active targeting together with the PEG leaded enhanced permeability and retention effect effect (passive targeting) enhances the accumulation of multifunctional nanoparticles in tumor. Importantly, the synthesized UCNP–PEG–FA/PC$_{70}$ may provide solutions to the two bottleneck problems of PDT, namely, limited penetration depth and oxygen-deficient microenvironment. These results highlight the potential of UCNP–PEG–FA/PC$_{70}$ as a multifunctional theranostic agent for imaging-guided PDT of tumor and a promising candidate for overcoming the problem of existing PDT agents in deep cancerous tissue under hypoxic conditions.

CONFLICT OF INTEREST

The authors declare no conflict of interest.

ACKNOWLEDGEMENTS

1 He, Q. & Shi, J. MSN anti-cancer nanomedicines: chemotherapy enhancement, overcoming of drug resistance, and metastasis inhibition. *Adv. Mater.* **26**, 391–411 (2014).
2 Chen, X., Gambhir, S. S. & Cheon, J. Theranostic nanomedicine. *Acc. Chem. Res.* **44**, 841 (2011).
3 Wang, J., Hu, Z., Xu, J. & Zhao, Y. Therapeutic applications of low-toxicity spherical nanocarbon materials. *NPG Asia Mater.* **6**, e84 (2014).
4 Tian, B., Wang, C., Zhang, S., Feng, L. & Liu, Z. Photothermally enhanced photodynamic therapy delivered by nano-graphene oxide. *ACS Nano* **5**, 7000–7009 (2011).
5 Ge, J., Lan, M., Zhou, B., Liu, W., Guo, L., Wang, H., Jia, Q., Niu, G., Huang, X., Zhou, H., Meng, X., Wang, P., Lee, C. S., Zhang, W. & Han, X. A graphene quantum dot photodynamic therapy agent with high singlet oxygen generation. *Nat. Commun.* **5**, 4596–4603 (2014).
6 Chen, D., Wang, C., Nie, X., Li, S., Li, R., Guan, M., Liu, Z., Chen, C., Wang, C., Shu, C. & Wan, L. Photoacoustic imaging guided near-infrared photothermal therapy using highly water-dispersible single-walled carbon nanohorns as theranostic agents. *Adv. Funct. Mater.* **24**, 6621–6628 (2014).
7 Liang, C., Diao, S., Wang, C., Gong, H., Liu, T., Hong, G., Shi, X., Dai, H. & Liu, Z. Tumor metastasis inhibition by imaging-guided photothermal therapy with single-walled carbon nanotubes. *Adv. Mater.* **26**, 5646–5652 (2014).
8 Dai, Y., Xiao, H., Liu, J., Yuan, Q., Ma, P., Yang, D., Li, C., Cheng, Z., Hou, Z., Yang, P. & Lin, J. In vivo multimodality imaging and cancer therapy by near-infrared light-triggered trans-platinum pro-drug-conjugated upconverison nanoparticles. *J. Am. Chem. Soc.* **135**, 18920–18929 (2013).
9 Zhu, H., Chen, H., Zeng, X., Wang, Z., Zhang, X., Wu, Y., Gao, Y., Zhang, J., Liu, K., Liu, R., Cai, L., Mei, L. & Feng, S. S. Co-delivery of chemotherapeutic drugs with vitamin E TPGS by porous PLGA nanoparticles for enhanced chemotherapy against multi-drug resistance. *Biomaterials* **35**, 2391–2400 (2014).
10 Shieh, M. J., Peng, C. L., Lou, P. J., Chiu, C. H., Tsai, T. Y., Hsu, C. Y., Yeh, C. Y. & Lai, P. S. Non-toxic phototriggered gene transfection by PAMAM-porphyrin conjugates. *J. Control Release* **129**, 200–206 (2008).
11 Yuan, H., Chong, H., Wang, B., Zhu, C., Liu, L., Yang, Q., Lv, F. & Wang, S. Chemical molecule-induced light-activated system for anticancer and antifungal activities. *J. Am. Chem. Soc.* **134**, 13184–13187 (2012).
12 Li, J., Cai, P., Shalviri, A., Henderson, J. T., He, C., Foltz, W. D., Prasad, P., Brodersen, P. M., Chen, Y., DaCosta, R., Rauth, A. M. & Wu, X. Y. A multifunctional polymeric nanotheranostic system delivers doxorubicin and imaging agents across the blood-brain barrier targeting brain metastases of breast cancer. *ACS Nano* **8**, 9925–9940 (2014).
13 Huang, P., Wang, D., Su, Y., Huang, W., Zhou, Y., Cui, D., Zhu, X. & Yan, D. Combination of small molecule prodrug and nanodrug delivery: amphiphilic drug-drug conjugate for cancer therapy. *J. Am. Chem. Soc.* **136**, 11748–11756 (2014).
14 Zhang, L., Gao, S., Zhang, F., Yang, K., Ma, Q. & Zhu, L. Activatable hyaluronic acid nanoparticle as a theranostic agent for optical/photoacoustic image-guided photothermal therapy. *ACS Nano* **8**, 12250–12258 (2014).
15 Fan, Q., Cheng, K., Yang, Z., Zhang, R., Yang, M., Hu, X., Ma, X., Bu, L., Lu, X., Xiong, X., Huang, W., Zhao, H. & Cheng, Z. Perylene-diimide-based nanoparticles as highly efficient photoacoustic agents for deep brain tumor imaging in living mice. *Adv. Mater.* **27**, 843–847 (2015).
16 Vijayaraghavan, P., Liu, C. H., Vankayala, R., Chiang, C. S. & Hwang, K. C. Designing multi-branched gold nanoechinus for NIR light activated dual modal photodynamic and photothermal therapy in the second biological window. *Adv. Mater.* **26**, 6689–6695 (2014).
17 Yuan, H., Wilson, C. M., Xia, J., Doyle, S. L., Li, S., Fales, A. M., Liu, Y., Ozaki, E., Mulfaul, K., Hanna, G., Palmer, G. M., Wang, L. V. & Vo-Dinh, T. Plasmonics-enhanced and optically modulated delivery of gold nanostars into brain tumor. *Nanoscale* **6**, 4078–4082 (2014).
18 Huang, P., Rong, P., Lin, J., Li, W., Yan, X., Zhang, M. G., Nie, L., Niu, G., Lu, J., Wang, W. & Chen, X Triphase interface synthesis of plasmonic gold bellflowers as near-infrared light mediated acoustic and thermal theranostics. *J. Am. Chem. Soc.* **136**, 8307–8313 (2014).
19 Wang, B., Wang, J. H., Liu, Q., Huang, H., Chen, M., Li, K., Li, C., Yu, X. F. & Chu, P. K. Rose-bengal-conjugated gold nanorods for in vivo photodynamic and photothermal oral cancer therapies. *Biomaterials* **35**, 1954–1966 (2014).
20 Wang, Y., Wang, H., Liu, D., Song, S., Wang, X. & Zhang, H. Graphene oxide covalently grafted upconversion nanoparticles for combined NIR mediated imaging and photothermal/photodynamic cancer therapy. *Biomaterials* **34**, 7715–7724 (2013).
21 Wang, L., Shi, J., Liu, R., Liu, Y., Zhang, J., Yu, X., Gao, J., Zhang, C. & Zhang, Z. Photodynamic effect of functionalized single-walled carbon nanotubes: a potential sensitizer for photodynamic therapy. *Nanoscale* **6**, 4642–4651 (2014).
22 Kalluru, P., Vankayala, R., Chiang, C. & Hwang, K. C. Photosensitization of singlet oxygen and in vivo photodynamic therapeutic effects mediated by PEGylated W(18)O (49) nanowires. *Angew. Chem. Int. Ed.* **52**, 12332–12336 (2013).
23 Cheng, L., Liu, J., Gu, X., Gong, H., Shi, X., Liu, T., Wang, C., Wang, X., Liu, G., Xing, H., Bu, W., Sun, B. & Liu, Z. PEGylated WS(2) nanosheets as a multifunctional theranostic agent for in vivo dual-modal CT/photoacoustic imaging guided photothermal therapy. *Adv. Mater.* **26**, 1886–1893 (2014).
24 Secret, E., Maynadier, M., Gallud, A., Chaix, A., Bouffard, E., Gary-Bobo, M., Marcotte, N., Mongin, O., Cheikh, K., El, Hugues, V., Auffan, M., Frochot, C., Morere, A., Maillard, P., Blanchard-Desce, M., Sailor, M. J., Garcia, M., Durand, J. O. & Cunin, F. Two-photon excitation of porphyrin-functionalized porous silicon nanoparticles for photodynamic therapy. *Adv. Mater.* **26**, 7643–7648 (2014).
25 Barreto, J. A., O'Malley, W., Kubeil, M., Graham, B., Stephan, H. & Spiccia, L. Nanomaterials: applications in cancer imaging and therapy. *Adv. Mater.* **23**, H18–H40 (2011).
26 Maji, S. K., Sreejith, S., Joseph, J., Lin, M., He, T., Tong, Y., Sun, H., Yu, S. W. & Zhao, Y. Upconversion nanoparticles as a contrast agent for photoacoustic imaging in live mice. *Adv. Mater.* **26**, 5633–5638 (2014).
27 Wang, F., Deng, R., Wang, J., Wang, Q., Han, Y., Zhu, H., Chen, X. & Liu, X. Tuning upconversion through energy migration in core-shell nanoparticles. *Nat. Mater.* **10**, 968–973 (2011).
28 Sun, L. D., Wang, Y. F. & Yan, C. H. Paradigms and challenges for bioapplication of rare earth upconversion luminescent nanoparticles: small size and tunable emission/excitation spectra. *Acc. Chem. Res.* **47**, 1001–1009 (2014).

29 Li, L. L., Zhang, R., Yin, L., Zheng, K., Qin, W., Selvin, P. R. & Lu, Y. Biomimetic surface engineering of lanthanide-doped upconversion nanoparticles as versatile bioprobes. *Angew. Chem. Int. Ed. Engl.* **51**, 6121–6125 (2012).

30 Feng, W., Zhu, X. & Li, F. Recent advances in the optimization and functionalization of upconversion nanomaterials for in vivo bioapplications. *NPG Asia Mater.* **5**, e84 (2013).

31 Qiao, X. F., Zhou, J. C., Xiao, J. W., Wang, Y. F., Sun, L. D. & Yan, C. H. Triple-functional core-shell structured upconversion luminescent nanoparticles covalently grafted with photosensitizer for luminescent, magnetic resonance imaging and photodynamic therapy in vitro. *Nanoscale* **4**, 4611–4623 (2012).

32 Zhang, P., Steelant, W., Kumar, M. & Scholfield, M. Versatile photosensitizers for photodynamic therapy at infrared excitation. *J. Am. Chem. Soc.* **129**, 4526–4527 (2007).

33 Park, Y. I., Kim, H. M., Kim, J. H., Moon, K. C., Yoo, B., Lee, K. T., Lee, N., Choi, Y., Park, W., Ling, D., Na, K., Moon, W. K., Choi, S. H., Park, H. S., Yoon, S. Y., Suh, Y. D., Lee, S. H. & Hyeon, T. Theranostic probe based on lanthanide-doped nanoparticles for simultaneous in vivo dual-modal imaging and photodynamic therapy. *Adv. Mater.* **24**, 5755–5761 (2012).

34 Wang, C., Cheng, L., Liu, Y., Wang, X., Ma, X., Deng, Z., Li, Y. & Liu, Z. Imaging-guided pH-sensitive photodynamic therapy using charge reversible upconversion nanoparticles under near-infrared light. *Adv. Funct. Mater.* **23**, 3077–3086 (2013).

35 Chen, Q., Wang, C., Cheng, L., He, W., Cheng, Z. & Liu, Z. Protein modified upconversion nanoparticles for imaging-guided combined photothermal and photodynamic therapy. *Biomaterials* **35**, 2915–2923 (2014).

36 Bratasz, A., Kulkarni, A. C. & Kuppusamy, P. A highly sensitive biocompatible spin probe for imaging of oxygen concentration in tissues. *Biophys. J.* **92**, 2918–2925 (2007).

37 Rieffel, J., Chen, F., Kim, J., Chen, G., Shao, W., Shao, S., Chitgupi, U., Hernandez, R., Graves, S. A., Nickles, R. J., Prasad, P. N., Kim, C., Cai, W. & Lovell, J. F. Hexamodal imaging with porphyrin-phospholipid-coated upconversion nanoparticles. *Adv. Mater.* **27**, 1785–1790 (2015).

38 Guan, M., Qin, T., Ge, J., Zhen, M., Xu, W., Chen, D., Li, S., Wang, C., Su, H. & Shu, C. Amphiphilic trismethylpyridylporphyrin-fullerene (C$_{70}$) dyad: an efficient photosensitizer under hypoxia condition. *J. Mater. Chem. B* **3**, 776–783 (2015).

39 Mai, H., Zhang, Y., Si, R., Yan, Z., Sun, L., You, L. & Yan, C. High-quality sodium rare-earth fluoride nanocrystals: controlled synthesis and optical properties. *J. Am. Chem. Soc.* **128**, 6426–6436 (2006).

40 Yin, A., Zhang, Y., Sun, L. & Yan, C. Colloidal synthesis and blue based multicolor upconversion emissions of size and composition controlled monodisperse hexagonal NaYF$_4$:Yb,Tm nanocrystals. *Nanoscale* **2**, 953–959 (2010).

Supplementary Information accompanies the paper on the NPG Asia Materials website (http://www.nature.com/am)